



Efficient rolling motion for snake-like robots utilizing center of gravity shift[☆]

Akio Yamano ^{*}, Yuuki Ikeda, Keita Imai, Masakatsu Chiba

Department of Aerospace Engineering, Graduate School of Engineering, Osaka Metropolitan University, 1-1 Gakuen-cho, Naka-ku, Sakai, 599-8531, Osaka, Japan

ARTICLE INFO

Keywords:

Biologically-inspired robots
Dynamics
Motion control
Snake-like robot
Rolling motion
Locomotion
Numerical simulation
Energy efficiency

ABSTRACT

Snake-like robots have attracted attention as robots that can travel over rough terrain where wheeled mobility mechanisms cannot. Previous research on snake-like robots has mainly focused on the biological movement of snakes; therefore, the issue of power consumption caused by driving a large number of actuators still remains unaddressed. In this study, we propose an efficient movement method using the movement of the center of gravity (COG) as a solution to the above-mentioned problem. In the proposed method, the snake-like robot is first transformed into a wheel shape, and then, some motors of the joint are moved to shift the COG and rotate the robot. Therefore, good movement efficiency can be achieved on leveled terrain by the rolling movement, and a snake-like undulating drive with high running performance can be selected on underwater and rough terrain. To realize the proposed movement method, we propose a method for switching between the rotational movement and undulation drive modes. However, the rolling motion with a COG shift needs a design of an appropriate orbit of the eccentric COG and timing of the motion stage transition. In this study, we demonstrate the rolling motion design with a simplified equation of motion. Next, experiments are conducted to verify the traveling efficiency in the proposed rolling mode, and it is proven that the method can achieve twice the traveling efficiency of the undulating motion.

1. Introduction

Currently, most robots that move on the ground have wheels. These wheeled mechanisms have the advantage of being more efficient and easier to control on smooth and level terrain than other ground-moving mechanisms. Conversely, the wheeled mechanism has the disadvantage of not being able to move on uneven or rocky terrain, narrow passages, and soft terrains such as sand or mud.

As a proposed mechanism to solve this problem, snake-like robots are attracting attention. A snake-like robot is a chordal robot with elongated links connected by many joints. By simultaneously moving multiple joints in various directions and angles, a snake-like robot can draw a smooth curve and move like a snake. Therefore, it can be used in all environments where snakes can move, such as rough terrain and in water, and is expected to play an active role in planetary exploration and disaster sites. For example, Enner et al. developed a robot that moves inside and outside a straight pipe, which can be used in a wide range of applications, such as the internal and external visual inspections of the pipe and non-destructive inspection [1]. Furthermore, in addition to adaptability to the environment, snake-like robots have various advantages over wheel-type and leg-type robots [2]. For example, a snake-like robot is robust against mechanical failures because of its modularity and redundancy, and it can be used as a manipulator by

fixing a part of its body [3]. Matsumoto et al. proposed the snake-like robot with a foldable arm that can rotate valves, open doors, access high places, and perform inspections in complex environments, such as factory plants [4].

The first quantitative study on snake migration was performed by Gray in 1946 [5], and, in 1972, Hirose created the first robot inspired by the movement of snakes [6]. The robot had a passive wheel attached to the bottom to model the motion of a real snake. However, while wheeled snake-like robots have advantages such as ease of modeling and control design, they are somewhat less adaptable to environmental changes; for example, their mobility gets affected in muddy water. Therefore, for the first time, modeling, feedback control, and power efficiency of meandering motion of a wheelless snake-like robot were analyzed by Sato et al. [2]. While wheelless snake-like robots are complex to model and control, they have the potential to fully reproduce the environmental adaptability of snakes. In addition, Ijspeert et al. proposed a control architecture for a wheelless snake-like robot that can move both underwater and on land [7]. In addition, Transeth et al. proposed a fast thrust method of moving over flat terrain using obstacles [8,9].

In another recent study, Kelasidi et al. experimentally investigated the relationship between the speed and power consumption of a snake-like robot moving in water, and examined the energy efficiency of a

[☆] This paper was recommended for publication by Associate Editor Qining Wang.

* Corresponding author.

E-mail address: yamano_aero@omu.ac.jp (A. Yamano).

Nomenclature	
e	Position vector of the COG from the rolling center O' on the inertial coordinate system
$r_{O'}$	Position vector of the rolling center O' from the origin O on the inertial coordinate system
$\Delta\psi$	Phase difference between each joint for the undulation
η	Traveling efficiency
μ	Rolling friction coefficients
ϕ_i	Relative joint angle of the i th link
ρ	Mass per unit area of the body under the rolling mode
θ	Rolling angle
c_{body}	Rotational damping coefficient of the joint
f	Frequency of the undulating locomotion
g	Gravitational acceleration
$J_{O'}$	Moment of inertia of the body at the rolling center O' under the rolling mode
k_{body}	Rotational spring constant of the joint
M	Total mass of the snake-like robot
N_{servo}	The number of servomotors required for lateral undulation
$O - XY$	Inertial coordinate system
$O' - x'y'$	Material coordinate system
P_{in}	Time-averaged consumed power
R	Radius of the body under the rolling mode
$u_{\text{in},i}$	Input torque at the i th joint for the undulation
V	Time-averaged velocity

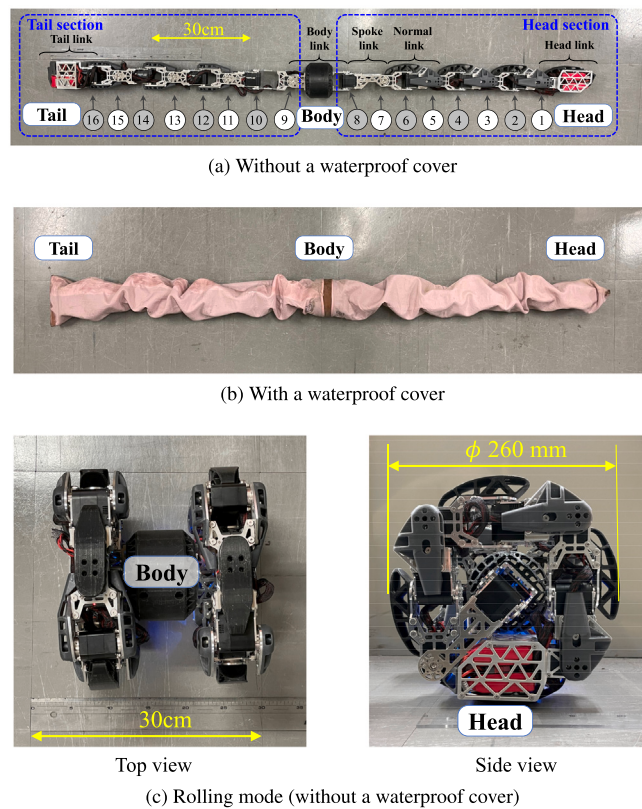


Fig. 1. Overview of the snake-like robot. (a) Without a waterproof cover. The main structure comprises duralumin, ABS, and tough resin, and it includes 16 servomotors as actuators. The number inside the circle represents the servomotor index. (b) With a waterproof cover. Body links are covered with a rubber and nylon cloth. (c) Rolling mode. Efficient rolling motion is generated by the COG shift.

swimming snake-like robot [10]. Yamano et al. experimentally identified the fluid force acting on a snake-like robot that swims in fluids of different viscosities and formulated a numerical analytical model for it [11]. Furthermore, Jia et al. proposed a method for avoiding obstacles in an uncertain environment using reinforcement learning and verified it with experiments and simulations [12]. In addition, Take-mori et al. realized the motion of passing through the hoop by switching the motion of the snake-like robot under different environments [13].

As an example of adding a self-reconfiguration function to a snake-like robot, Kurokawa et al. developed a robot called M-TRAN, which can change its own configuration. By using a mechanism with many degrees of freedom and a self-reconfiguration function, they were able to realize several types of motions, such as crawling, quadrupedal walking, and caterpillar-like motion. This allows the robot to perform adaptive movements in unpredictable environments. The system is also expected to have a long service life because of its homogeneity, which makes it possible to replace a damaged module with another one [14]. Zhao et al. developed a similar reconfigurable robot, UBot, in which each module of the one has a cubic structure based on universal joints, with two rotational degrees of freedom and four connection surfaces, and can connect and disconnect from adjacent modules. Subsequently, three movement modes — snake, quadruped, and loop — were realized [15]. Wang et al. proposed the serpenoid polygon model, which is an extension of the serpenoid curve, as a simple method to plan the angle of each joint for the rotational movement of the reconfigurable robot. The effectiveness of the model was experimentally verified using the UBot modular robot [16].

The above studies focused on biological snake locomotion to verify movement efficiency and stability. Conversely, snake-like robots have

the disadvantage of low movement speeds and a lower energy efficiency than that of wheeled robots owing to the need to simultaneously drive a large number of actuators. Because many actuators of the joints are moved and operated, a significant improvement in energy efficiency cannot be expected. As an example of the reconfigurable snake-like robot, fast movement on flat terrain has been achieved by selecting the loop-shaped movement form [14–16]. However, in the rotational movement of the loop structure, it is still necessary to drive all the joints that realize the dorsal deformation to deform the loop shape and generate the rotational motion. In contrast, in this study, we propose a new efficient method of locomotion that is applicable to snake-like robots. We attempt to improve the movement efficiency of the wheelless snake-like robot on the flat ground, and propose a method of improving the movement efficiency by transforming the snake-like robot into a shape of a wheel to enable it to move by rolling. The robot first transforms from a snake-like shape to a wheel shape, and then shifts its center of gravity (COG) forward by moving its joints in that state. This is expected to reduce the number of motors used for movement while maintaining both low power consumption and high propulsion efficiency. In addition, because it rotates in a near-perfect circle, it is expected to improve the travel efficiency by significantly reducing rolling friction on level ground.

We present an experimental model of a snake-like robot that transforms into a wheel and verify the improvement of the traveling efficiency through experiments and simulations. The remainder of this paper is organized as follows: Chapter 2 describes the overview of the experimental model. Chapter 3 presents the control method for the undulation of the conventional method of the snake-like robot, the proposed rolling motion for more efficient drive, and the methodology of motion transformation between undulation and rolling. Chapter 4

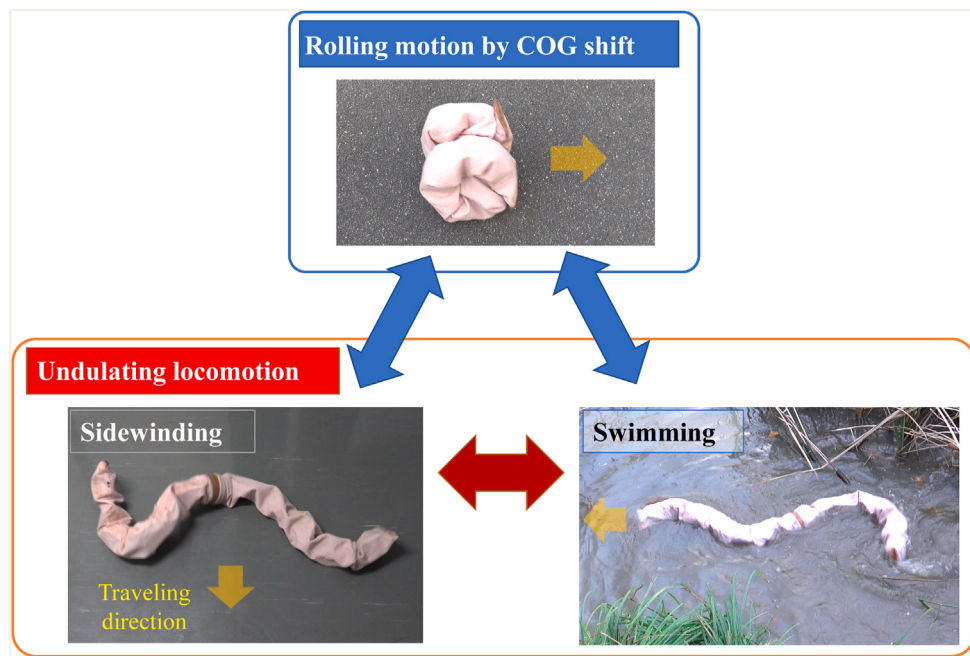


Fig. 2. Overview of the locomotion modes. The rolling motion is generated by COG shift with the transformation of multi-links, and this mode helps achieve high traveling efficiency on even ground. The undulation, including the sidewinding and swimming locomotion, helps achieve high running performance on uneven ground and in fluid. However, the consumed power increases in these modes.

presents the design method for the rolling motion with a simplified mathematical model of the equation of motion. Chapter 5 describes the experimental setup and procedure to evaluate the proposed rolling motion. Chapter 6 presents the comparison of velocity and traveling efficiency between the undulation and the rolling motion. Finally, Chapter 7 presents the concluding remarks.

2. System overview

This section describes the specifications and control system of the experimental model of the proposed snake-like robot.

2.1. Body structure

The snake-like robot used in the experiment is illustrated in Fig. 1, and its specifications are listed in Table 1. This snake-like robot is composed of duralumin and an ABS resin, and 16 servomotors (B3M-SC-1170-A, KondoKagaku, Co., Ltd., Japan) are mounted as joint actuators, as illustrated in Fig. 1(a). The servomotors are arranged such that the rotation axes are staggered by 90° to enable three-dimensional motion. In addition, the robot is powered by 5200 mAh Li-Po batteries so that it can operate without a wired external power supply, which is often seen in other snake-like robots. Furthermore, the waterproof and dustproof properties are maintained by the waterproof cover made of rubber and nylon, as illustrated in Fig. 1(b).

Fig. 1(c) illustrates the body structure in the rolling mode. Servomotors transform the head and tail sections into a wheel shape using position control with PID control; subsequently, the snake-like robot is transformed into a shape of parallelized two wheels. The head and tail are designed to be on the same side when the snake-like robot is transformed into a wheel shape. Because the head and tail are heavier than other links, they are positioned directly below the transformed structure owing to gravity.

Fig. 2 displays the motion modes that can be realized using the proposed robot. The rolling motion is generated by COG shift with the transformation of multi-links, and this mode helps achieve high traveling efficiency on even ground. The undulation, including the sidewinding [17–20] and swimming locomotion [10,11], helps achieve

Table 1
Specifications of the snake-like robot.

Length	Total	1.66 m
	Head/Tail link	150 mm
	Normal link	160 mm × 6
	Spoke link	120 mm × 2
	Body link	157 mm
Mass	Total	5.63 kg
	Head/Tail link	420 g
	Battery	391 g
	Normal link	433 g × 6
	Spoke link	198 g × 2
	Body link	462 g
	Waterproof cover	912 g
Wireless modules	Number of joints	16
	Output torque	4.0 Nm (typical) 7.6 Nm (max)
	Main material	Duralumin, ABS, Tough resin
Component parts	Wireless modules	XBee, Digi International, US
	Actuator	KondoKagaku, Co., Ltd., Japan B3M-SC-1170-A ×16
	Power supply	KYPOM, Co., Ltd., China Li-Po battery 11.1 V 1,300 mAh ×4
	MCU	NXP, Inc., Nederland LPC1768 iMXRT1062

high running performance on uneven ground and in fluid. However, the consumed power increases in these modes.

2.2. Control system

Next, the control system of the robot is explained. Fig. 3 illustrates the overview of the control system for the snake-like robot. As shown in Fig. 3(a), the head and tail links include two batteries and a control circuit, respectively. The body link includes a control circuit and a

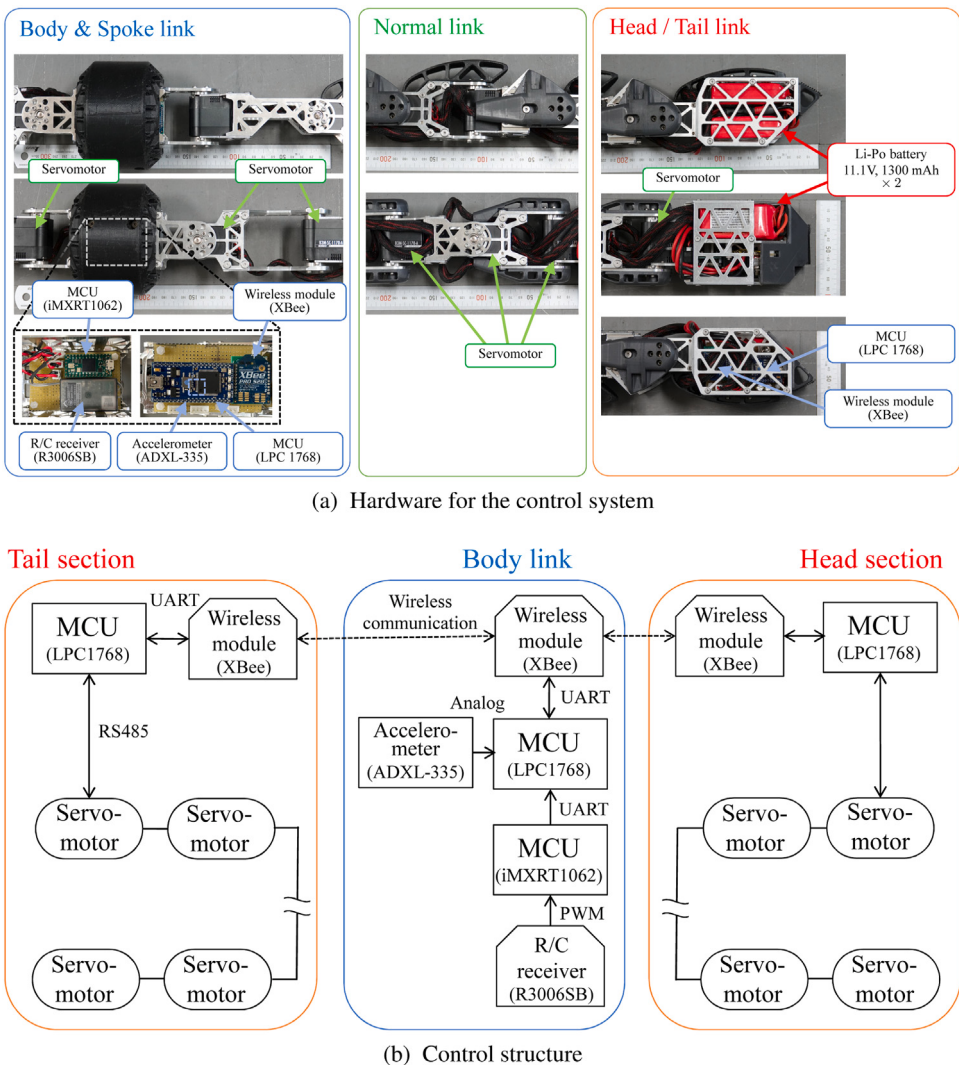


Fig. 3. Overview of the control system for the snake-like robot. First, the control signal is transmitted by the operator via a hand-radio controller to a radio receiver mounted on the body. Subsequently, the control signals are transmitted to the wireless modules (XBee, Digi International, US) on the head and tail of the snake-like robot. Finally, the motion is generated by the servomotors in the head and tail sections based on the command received via the wireless modules. The accelerometer in the body (ADXL-335, Analog Devices, US) is employed to generate the rolling motion.

radio receiver. Moreover, as shown in Fig. 3(b), the structure of the control system consists of three sections: head and tail sections, and the body link. First, the control signal is transmitted by the operator, via a hand-radio controller, to a radio receiver mounted on the body. Subsequently, the control commands for the head and tail sections are selected based on the signals received by the radio receiver on the body, and the control signals are transmitted to the wireless receivers (XBee, Digi International, US) on the head and tail of the snake-like robot with the period, 50 ms. Finally, the head and tail motion is generated with the control period, 30 ms, based on the command.

The micro-controller unit (MCU) (LPC1768, NXP, Inc., Nederland) in the head and tail links transmits the target torque command to the servomotor for the snake-like undulation. Inside the servomotor, PI control is performed so that the target torque command and output torque match based on current [11]. Torque control based on current prevents a current larger than the given current value flowing through the motor. This prevents damage of the motor and control circuit due to overloads on the servomotor, even during the undulating motion on uneven terrain with many obstacles.

In the rolling mode, the deformation to a tire shape is performed by the position control with PID control. The position control of the high-torque servomotor maintains an accurate circular tire shape, leading to

reduced losses during the rolling motion. The rotation angle is detected by the accelerometer (ADXL-335, Analog Devices, US) of the body after the wheel shape is formed. By sending a control command to the wireless receiver in the head and tail when the head and tail are positioned directly below the transformed structure, the movement of the COG is realized and the rotational motion is generated. The right (head section) and left wheels (tail section) are mounted in opposite directions. This allows the robot to move forward by moving the head section and backward by moving the tail section. When turning, the snake-like robot turns by the undulating mode; subsequently, the body again deforms into the tire shape.

The relative angle, current, and voltage values of each servomotor are acquired with a 30 ms period using the MCU in the head and tail links. Then, the consumed power of the servo motors is calculated from the current and voltage values. These data, together with the rolling angle measured in the body link, are logged in the Flash ROM in the MCU as the short-int type binary data to speed up the logging speed. The recording is started and stopped using a hand-radio controller. The binary data logged in the MCU are post-processed and visualized using MATLAB (The MathWorks, Inc., USA).

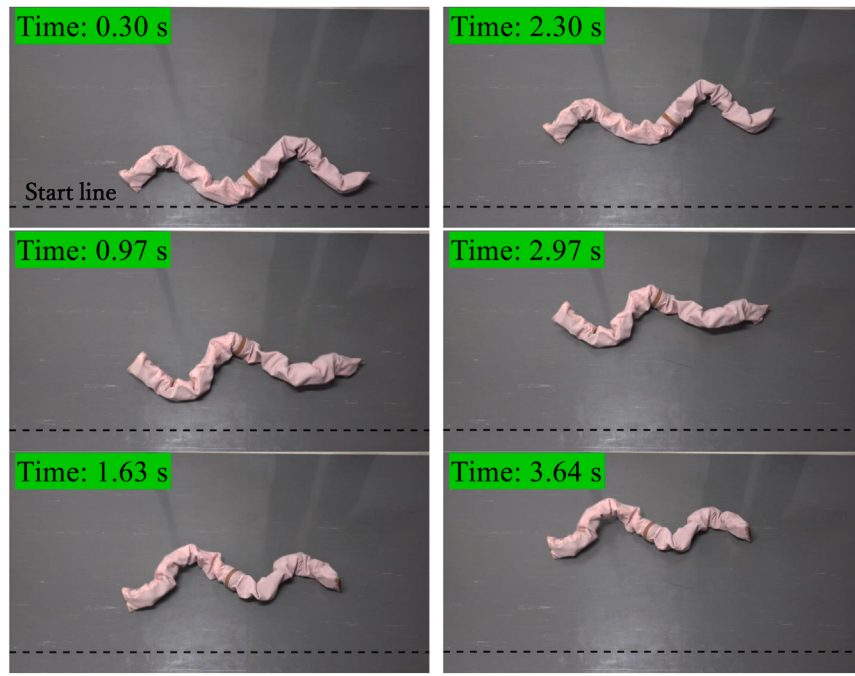


Fig. 4. Sidewinding locomotion of the snake-like robot (with waterproof cover). These locomotions are generated by parameters $f = 0.5$ Hz, $\Delta\psi = \pi/2.5$ rad, $u_{\max,h} = 15$ Nm, and $u_{\max,v} = 8$ Nm.

3. Motion control

This section presents the control method for undulation as a conventional method for the snake-like robot, the proposed rolling motion with the COG shift for a more efficient drive, and the methodology of motion transformation between undulation and rolling.

3.1. Sidewinding locomotion

In this section, we demonstrate the sidewinding locomotion as one of the conventional undulations for the snake-like robot.

Sidewinding locomotion is a type of undulating locomotion used by rattlesnakes to move across sandy environments. This peculiar gait is a movement in which the body is lifted by a vertical undulation; the part of the body that touches the ground and the part that is lifted from the ground are alternately exchanged, and the body moves forward through lateral undulation. Sidewinding is expected to be useful because it can realize complicated turning motions by a simple method of superimposing horizontal and vertical undulations without passive wheels [17]. In addition, because the vertical undulation can control the ground and non-ground planes, sidewinding is expected to enable movement on rugged terrain [18].

Tesch et al. compared the energy consumptions during sidewinding locomotion and other undulating locomotions, and sidewinding demonstrated a high energy efficiency [19]. Furthermore, Ariizumi et al. reported the relationship between the movement speed and energy efficiency, investigated by numerical analyses for three locomotions of snakes in different frictional environments: lateral undulation, sinus-lifting motion, and sidewinding locomotion. Furthermore, it has been clarified that the sidewinding locomotion is the most efficient in an environment where the anisotropy of friction is not sufficiently large [20].

In our study, sidewinding locomotion is generated by superimposing the horizontal and vertical undulations with the torque control of servomotors. The target torque, $u_{t,m}$, of the m th servomotor for horizontal and vertical undulations, $m \in \{1, \dots, N_{\text{servo}}\}$, is defined to realize the sidewinding locomotion of the snake-like robot, with the number of

servomotors required for undulation, N_{servo} , being sixteen. Thus, the target torque at time t can be defined as

$$u_{t,m} := -k_{\text{body}}\phi_{o,m} - c_{\text{body}}\dot{\phi}_{o,m} + u_{\text{in},m}(t), \quad (1)$$

$$u_{\text{in},2n-1}(t) := u_{\max,h} \sin(2\pi f t - (n-1)\Delta\psi), \quad (2)$$

$$u_{\text{in},2n}(t) := u_{\max,v} \cos(2\pi f t - (n-1)\Delta\psi), \quad (3)$$

$n \in \{1, \dots, N_{\text{servo}}/2\}$, where, $k_{\text{body}} = 180 \times 10^{-3}$ Nm/degree is the rotational spring constant on the joint, and $c_{\text{body}} = 0.05 \times 10^{-3}$ sNm/degree is the damping coefficient on the joint. These terms emulate the effect of the rotational spring and the rotational damping at each joint, respectively. The constants were determined such that relative joint angles would stay within the limits of a joint angle while the snake-like robot undulates. The observed relative joint angle, $\phi_{o,m}$, is measured using a rotary encoder in a servomotor.

Moreover, $u_{\max,h}$ and $u_{\max,v}$ are the amplitudes of the input torque for horizontal and vertical undulations, respectively. $\Delta\psi$ is the phase difference between each joint required to generate undulation. Parameter f denotes the frequency of the locomotion.

Fig. 4 illustrates the sidewinding locomotion generated by Eqs. (1)–(3) with parameters $f = 0.5$ Hz, $\Delta\psi = \pi/2.5$ rad, $u_{\max,h} = 15$ Nm, and $u_{\max,v} = 8$ Nm.

3.2. Rolling motion with the COG shift

We propose the rolling motion with a COG shift as more efficient motion than other locomotions.

Fig. 5 demonstrates the proposed rolling motion with the COG shift. **Fig. 5(a)** illustrates the procedure of the rolling motion. The procedure of this motion is divided into four stages as follows:

- [Step 1] Kick stage: The head or tail section is moved to kick the ground, to generate the rolling motion.
- [Step 2] COG shift stage I: A heavier head or tail link is moved forward to move the COG forward.
- [Step 3] COG shift stage II: A heavier head or tail link is moved above to move the COG forward.
- [Step 4] Rolling stage: Rolling motion is generated by gravity.

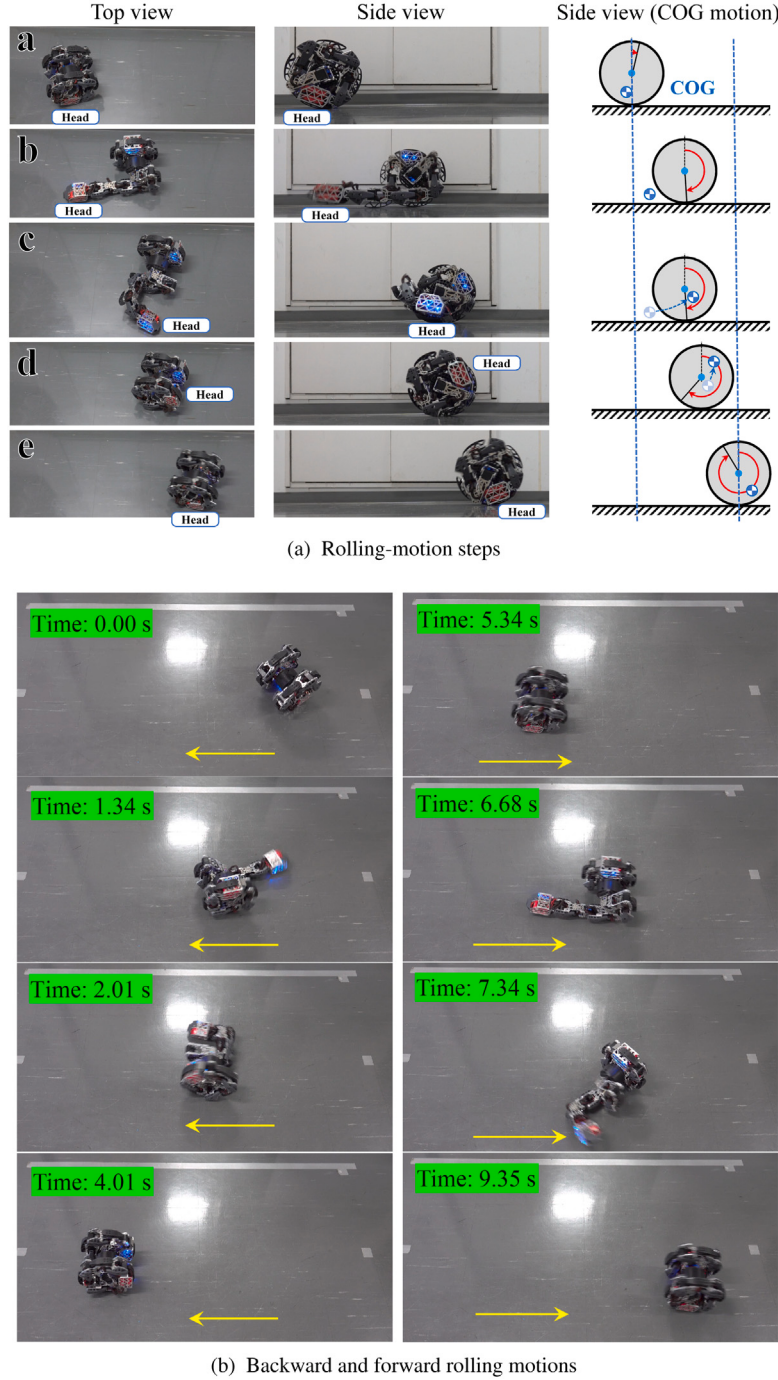


Fig. 5. Rolling motion by the COG shift of the snake-like robot (without a waterproof cover). Above figures show the (a) initial state, (b) kick stage, (c) COG-shift stage I, (d) COG-shift stage II, and (e) rolling stage. Below figures show the backward and forward rolling motions.

The operation from [Step 1] to [Step 3] is executed under the following conditions for the rotation angle θ_o measured by the accelerometer, which is $\theta_o = 0$ in the initial state,

$$\theta_o \in \{\theta \in \mathbb{R} \mid \theta_{\min} + 2n\pi < \theta \leq \theta_{\max} + 2n\pi, n \in \mathbb{Z}\}, \quad (4)$$

where θ_{\max} and θ_{\min} represent the limits of the control parameter used to design the appropriate timing for the kick stage. In this motion, the body is formed as a wheel, as illustrated in Fig. 1(c), and the rolling motion is generated by gravity acting on the eccentric COG. Therefore, the traveling efficiency is better than other undulating locomotions which need to drive all servomotors. Moreover, Fig. 5(b) illustrates the

backward and forward rolling motions. The robot can move forward by moving the head link and backward by moving the tail link.

However, the rolling motion with the COG shift needs to design an appropriate orbit of the eccentric COG and timing of the motion stage transition. We demonstrate the above-mentioned design method with a simplified equation of motion in the next chapter.

3.3. Methodology of motion transformation

Fig. 6(a) displays the snapshot of the motion transformation from the undulation to the rolling mode. After shifting from the undulating motion to the rolling mode, the control mode of the servomotor is

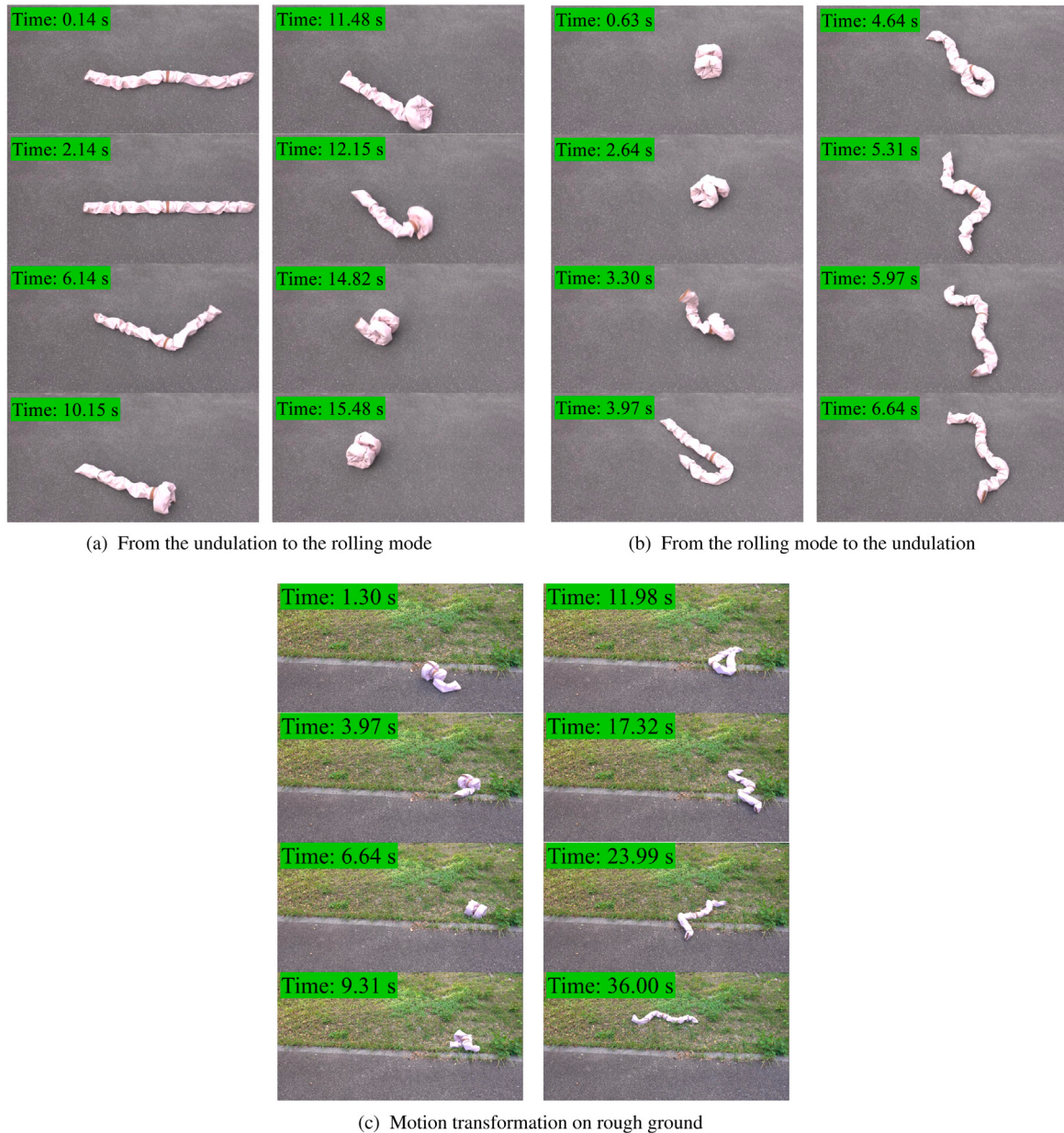


Fig. 6. Snapshots of the motion transformation (with a waterproof cover) (a) from the undulation to the rolling mode and (b) from the rolling mode to the undulation. (c) The motion transformation from the rolling mode to the undulation achieves the traveling on the grass where the rolling mode cannot travel, as shown in 6.64 s.

changed from the torque control to the position control. The following target relative angle $\phi_{d,m}$, $m \in \{1, \dots, N_{\text{servo}}\}$ is given to the head section when transitioning to the rolling mode,

$$\phi_{d,m}(t) = \begin{cases} 0, & \psi_{d,m}(t) < 0, \\ \phi_{\max,m}, & \phi_{\max,m} < \psi_{d,m}(t), \\ \psi_{d,m}(t), & \text{otherwise,} \end{cases} \quad (5)$$

$$\psi_{d,m}(t) := \omega_r \left(t - \frac{7-m}{2} \right), \quad (6)$$

where $\omega_r = 50$ degree/s and $[\phi_{\max,m}] = [90 \ 0 \ 90 \ 0 \ 90 \ 0 \ 135 \ 90]$ degree. The tail section is given the following target relative angles $\phi_{d,m}$, $m \in \{N_{\text{servo}} + 1, \dots, 2N_{\text{servo}}\}$,

$$\phi_{d,m}(t) := \phi_{d,2N_{\text{servo}}-m+1}(t-6). \quad (7)$$

Next, Fig. 6(b) shows the snapshot of the motion transformation from the rolling mode to the undulation. The control mode of the

servomotor is changed to torque control during undulation. The virtual-rotational-spring term in Eq. (1) provides a smooth motion transition from the rolling mode with complex shapes to the undulating motion.

Fig. 6(c) illustrates the motion transformation on rough ground where the rolling mode cannot travel. The motion transformation from the rolling mode to the undulation achieves the traveling on the grass where the rolling mode cannot travel as shown in 6.64 s.

4. Design of the rolling motion with a mathematical model

To achieve the rolling motion, it is necessary to design an appropriate orbit for the eccentric COG and the timing of the motion stage transition. However, the search in experiments for appropriate driving conditions from a wide range of control parameters requires significant time and effort. Because the simplified equation of motion is computationally inexpensive, it is easier to search for appropriate driving conditions among a wide range of control parameters by simulation on a computer.

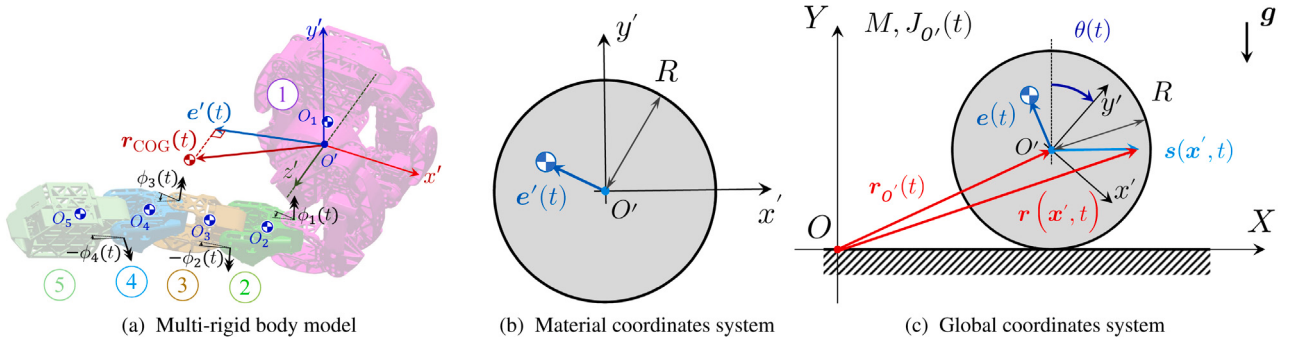


Fig. 7. Overview of the simplified mathematical model, and definition of the global and material coordinates. **(a)** The snake-like robot under the rolling mode is a multi-link mechanism, and it can be considered to be composed of five rigid bodies. Then, the motion of the COG r_{COG} during the rolling motion is represented by a trajectory in three dimensions. **(b)** Next, the trajectory of the COG e' projected on the 2D disk is considered on material coordinate system $O'-x'y'$. **(c)** Finally, the equation of motion for the rolling mode is modeled by the eccentric cylinder under the nonslip assumption on global coordinate system $O-XY$.

We demonstrate how to design an appropriate orbit of the eccentric COG and timing of the motion stage transition by using a simplified equation of motion in this chapter.

4.1. Equation of motion

Fig. 7 shows the overview of the simplified mathematical model, the definition of the global coordinates $O-XY$ (**Fig. 7(c)**), and the material coordinates on the rolling body $O'-x'y'$ (**Fig. 7(b)**). In this section, we derive a simplified equation of motion by introducing the following assumptions;

- [Asm. 1] Eccentric disk approximation: A snake-like robot is a multi-link mechanism. Usually, the multi-body dynamics formulation is used to model the dynamics of the multi-link mechanism. However, this formulation is computationally expensive. Because the tire shape is maintained by the position control using high-torque servomotors, the body can be considered as a single rigid body. Therefore, the system is assumed to be an eccentric disk and modeled as a one-degree-of-freedom system with low computational cost.
- [Asm. 2] Two dimensional COG motion: The motion of the COG during the rolling motion is represented by a trajectory in three dimensions, as shown in **Fig. 7(a)**. The trajectory of the COG projected on the 2D disk is considered, as shown in **Fig. 7(b)**, assuming that the motion of the COG does not affect the axial motion of the tire-shaped body during the rolling motion.
- [Asm. 3] Non-slip condition: Slip is unlikely to occur because of the rolling motion caused by the COG shift. Therefore, we consider the constraint condition of non-slip between the ground and tire-shaped body in the rolling motion.
- [Asm. 4] Ignore joint dynamics: The COG shift is achieved by deformation of the joints by servomotors. The servomotor has a high torque output, and the time constant of the joint dynamics is sufficiently small during position control. Therefore, the joint is assumed to deform according to the given time history of the target joint angle.

The snake-like robot under the rolling mode, illustrated in **Fig. 1(c)**, is modeled by the eccentric cylinder with the nonslip assumption, as shown in **Fig. 7(c)**. The radius, mass, and moment of inertia around the rotation center are R , M , and $J_{O'}(t)$, respectively. The gravity acting on the eccentric COG $e(t)$ generates the rolling motion.

Let $\mathbf{r}(\mathbf{x}', t)$ be the position in the global coordinate system corresponding to the position $\mathbf{x}' \in A$ on the material coordinates in the cylinder $A := \{\mathbf{x}' \in \mathbb{R}^2 \mid x'^2 + y'^2 \leq R^2\}$. The kinetic energy T is expressed as follows:

$$T(t) = \frac{1}{2} \int_A \rho(\mathbf{x}', t) \left| \frac{d\mathbf{r}(\mathbf{x}', t)}{dt} \right|^2 dA$$

$$= \frac{1}{2} \int_A \rho(\mathbf{x}', t) \left\{ \left| \frac{d\mathbf{r}_{O'}(t)}{dt} \right|^2 + \left| \frac{ds(\mathbf{x}', t)}{dt} \right|^2 + 2 \frac{ds(\mathbf{x}', t)^T}{dt} \frac{d\mathbf{r}_{O'}(t)}{dt} \right\} dA, \quad (8)$$

where $\rho(\mathbf{x}', t)$ is the mass per unit area of the rolling body. From the relationship between the global and material coordinate systems, the following relationship is obtained:

$$\mathbf{s}(\mathbf{x}', t) = \mathbf{R}(\theta(t))\mathbf{x}', \quad (9)$$

where $\mathbf{R}(\cdot) \in \mathbb{R}^{2 \times 2}$ is the rotation matrix. From Eqs. (8) and (9), we obtain

$$T(t) = \frac{1}{2} \int_A \rho(\mathbf{x}', t) \left[\left| \frac{d\mathbf{r}_{O'}(t)}{dt} \right|^2 + |\mathbf{x}'|^2 \left\{ \frac{d\theta(t)}{dt} \right\}^2 + 2\mathbf{x}'^T \mathbf{R} \left(\theta(t) + \frac{\pi}{2} \right) \frac{d\mathbf{r}_{O'}(t)}{dt} \frac{d\theta(t)}{dt} \right] dA. \quad (10)$$

From the definitions of mass M and COG on the material coordinates e' shown in **Fig. 7(b)**,

$$M = \int_A \rho(\mathbf{x}', t) dA, \quad M\mathbf{e}'(t) = \int_A \rho(\mathbf{x}', t) \mathbf{x}' dA. \quad (11)$$

Finally, the following form is obtained:

$$T(t) = \frac{1}{2} M \left| \frac{d\mathbf{r}_{O'}(t)}{dt} \right|^2 + \frac{1}{2} J_{O'}(t) \left\{ \frac{d\theta(t)}{dt} \right\}^2 + M\mathbf{e}'(t)^T \mathbf{R} \left(\theta(t) + \frac{\pi}{2} \right) \frac{d\mathbf{r}_{O'}(t)}{dt} \frac{d\theta(t)}{dt}. \quad (12)$$

Potential energy by gravity U is expressed as

$$U(t) = - \int_A \rho(\mathbf{x}', t) \mathbf{s}(\mathbf{x}', t)^T \mathbf{g} dA = -M\mathbf{e}'(t)^T \mathbf{R}(\theta(t))\mathbf{g}, \quad (13)$$

where $\mathbf{g} = [0 \ g]^T$ is the gravitational acceleration.

Nonslip constraint condition is denoted as

$$\mathbf{C} := \mathbf{r}_{O'}(t) - \mathbf{R} \begin{bmatrix} \theta(t) \\ 1 \end{bmatrix} = \mathbf{0}. \quad (14)$$

From Lagrange's equations with Eqs. (12), (13), and (14), the equation of motion is obtained as

$$\frac{d}{dt} \left(\frac{\partial L}{\partial \dot{q}} \right) - \frac{\partial L}{\partial q} = \lambda^T \frac{\partial \mathbf{C}}{\partial q} + \mathbf{f}, \quad (15)$$

$$\Leftrightarrow \left\{ J_{O'}(t) + MR^2 + 2MR\mathbf{e}'(t)^T \begin{bmatrix} -\sin \theta \\ \cos \theta \end{bmatrix} \right\} \ddot{\theta} + \left\{ J_{O'}(t) + 2MR\mathbf{e}'(t)^T \begin{bmatrix} -\sin \theta \\ \cos \theta \end{bmatrix} \right\} \dot{\theta} + \mu MgR \operatorname{sgn} \dot{\theta} - \{ MR\dot{\theta}^2 + Mg \} \mathbf{e}'(t)^T \begin{bmatrix} \cos \theta \\ \sin \theta \end{bmatrix} = 0, \quad (16)$$

where $L := T - U$ is Lagrangian, $\mathbf{q} := [r_{O'}^T \theta]^T \in \mathbb{R}^3$ represents the generalized coordinates, and $f := [\mathbf{0} - \mu M g R \operatorname{sgn} \dot{\theta}] \in \mathbb{R}^3$ is the drag caused by the frictional force. We search the appropriate orbit of COG on the material coordinates $e'(t)$ and timing of the motion stage transition from Eq. (16).

4.2. Numerical method for the rolling motion

The rolling motion comprises four stages of the motion transition, as illustrated in Section 3.2. Therefore, the equation of motion is switched according to the motion stage as follows:

- [Step 1] Kick stage: The control time τ is incremented while Eq. (4) is satisfied, the desired rolling angular velocity $\omega_d(\tau)$ is given while $\tau \in [0, \tau_1]$ and the following dynamics are solved:

$$\frac{d}{dt} \mathbf{x}(t) = \begin{bmatrix} \omega_d(\tau) \\ \dot{\omega}_d(\tau) \end{bmatrix}, \quad (17)$$

where $\mathbf{x} := [\theta \dot{\theta}]^T$ is the state variable.

- [Step 2] COG shift stage I, II: The following dynamics from Eq. (16) are solved under the given COG orbit $e'(t) = e'_d(t)$ and the time-series of the moment of inertia $J_{O'}(t) = J_{O',d}(t)$, $\tau \geq \tau_1$,

$$\frac{d}{dt} \mathbf{x}(t) = f(\mathbf{x}, t), \quad (18)$$

where, $e'_d(\cdot)$, $J_{O',d}(\cdot)$ are desired values, and

$$f(\mathbf{x}, t) := \begin{bmatrix} \dot{\theta} \\ \mathcal{J}(\theta, t)^{-1} \left\{ -C(\theta, \dot{\theta}, t) - \mathcal{K}(\theta, \dot{\theta}, t) \right\} \end{bmatrix}, \quad (19)$$

$$\mathcal{J}(\theta, t) := J_{O'}(t) + M R^2 + 2 M R e'(t)^T \begin{bmatrix} -\sin \theta \\ \cos \theta \end{bmatrix}, \quad (20)$$

$$C(\theta, \dot{\theta}, t) := \left\{ J_{O'}(t) + 2 M R e'(t)^T \begin{bmatrix} -\sin \theta \\ \cos \theta \end{bmatrix} \right\} \dot{\theta} + \mu M g R \operatorname{sgn} \dot{\theta}, \quad (21)$$

$$\mathcal{K}(\theta, \dot{\theta}, t) := -\{ M R \dot{\theta}^2 + M g \} e'(t)^T \begin{bmatrix} \cos \theta \\ \sin \theta \end{bmatrix}. \quad (22)$$

- [Step 3] Rolling stage: The control time τ is set to 0 s and solves the dynamics shown in Eq. (18) under COG $e'(t) = e'_d(0)$ and moment of inertia $J_{O'}(t) = J_{O',d}(0)$ if Eq. (4) is not satisfied.

The COG orbit $e'(t)$ and time-series of the moment of inertia $J_{O'}(t)$ are obtained from the function which is linearly interpolated in time with the values calculated from the CAD model for the shape of each motion stage. The COG velocity $\dot{e}'(t)$ and time-change rate of the moment of inertia $\dot{J}_{O'}(t)$ are calculated by the central difference of $e'(t)$ and $J_{O'}(t)$, respectively.

4.3. Case study of the rolling motion

In this section, we demonstrate the case study for the rolling motion, which is composed of various body shape transitions.

Fig. 8 illustrates the COG position e' and the moment of inertia $J_{O'}$ calculated by the CAD model (Inventor, Autodesk, US) for the shape of each motion stage of the rolling motion. The movement of the COG during the rolling motion is generated by the combination of these body shapes. Therefore, we evaluated the feasibility of the rolling motion by the following motion transitions using the simplified equations of motion: Eqs. (17) and (18).

[Case 1] (a) → (c) → (a).

[Case 2] (a) → (b) → (c) → (a).

where, [Case 1] represents the rolling motion generated only by the kicking motion, and [Case 2] shows the rolling motion generated by the kicking and the COG-shift motion.

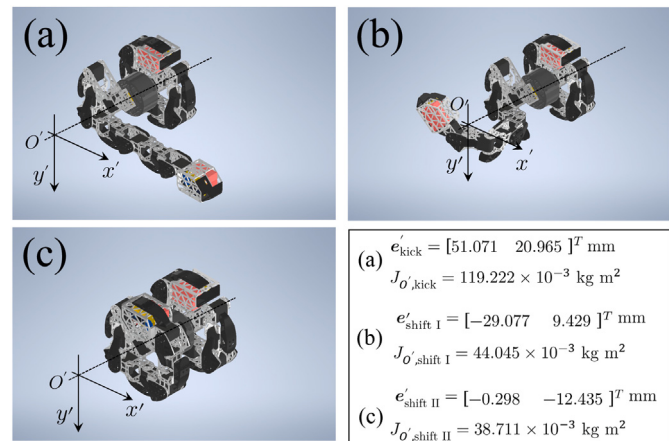


Fig. 8. COG position e' and the moment of inertia $J_{O'}$ calculated by the CAD model for the shape of each motion stage; (a) kick stage (e'_kick , $J_{O',\text{kick}}$), (b) COG shift stage I ($e'_\text{shift I}$, $J_{O',\text{shift I}}$), (c) COG shift stage II ($e'_\text{shift II}$, $J_{O',\text{shift II}}$).

The coefficient of rolling friction μ in Eq. (21) was identified from the free-rolling-motion experiment under various initial velocities in the shape illustrated in Fig. 8(c) using the following procedure: First, the angular velocity during the rolling motion is calculated from the measured time-series of the rolling angle during the free-rolling motion after a certain initial angular velocity is given. Then, the obtained angular velocity is given as the initial value in the simulation. Next, we search for a rolling-friction coefficient μ such that the difference between the simulated time-series of the rotation angle $\theta(t)$ and the measured time-series of the rotation angle is small. The validity of the identified rolling friction coefficients is confirmed by comparing the simulation results obtained using the identified rolling-friction coefficients and measurement results for the free-rolling motion for a different initial angular velocity.

Fig. 9 illustrates the comparison of the time-series of the rolling angle $\theta(t)$ during three trials of the free-rolling motion between experiments (red dashed line) on the smooth floor without (Fig. 9(a)) and with a waterproof cover (Fig. 9(b)), the asphalt pavement with a waterproof cover (Fig. 9(c)), and numerical analytical results (blue solid line) under the identified friction coefficient, respectively. Here, the rotation angle in the experiment was calculated using the phase shift from the following equation based on accelerations measured by the accelerometer (ADXL-335, Analog Devices, US) in the body link,

$$\tilde{\theta}_o = \arctan 2(a_{y'}, a_{x'}) \in [-\pi, \pi], \quad (23)$$

where $a_{x'}$ and $a_{y'}$ are the acceleration components of the x' and y' axes, respectively.

The identified rolling-friction coefficients displayed in Fig. 9 are $\mu = 0.016$ on the smooth floor without the cover, 0.025 on the smooth floor with the cover, and 0.030 on the asphalt pavement with the cover. These numerical results show good agreement with the experimental results; however, the experimental results indicate that a steady-state error occurs when the rotational motion is stopped. This is because the body shape during the rolling mode, as illustrated in Fig. 1(c), is not a perfect circle, and the dent on the body stops the rotational movement during the free-rolling motion.

Fig. 10 shows the time-series of the rolling angle $\theta(t)$ obtained by numerical analysis under the above-mentioned motion transitions: [Case 1], [Case 2], and various rolling friction coefficients μ . We employed the following control law in Eq. (4):

$$\theta_{\min} = -\frac{\pi}{4} \text{ rad}, \theta_{\max} \in \left\{ \pi, \frac{13}{12}\pi, \frac{5}{4}\pi, \frac{3}{2}\pi \right\} \text{ rad}. \quad (24)$$

Moreover, the desired rolling angular velocity for the numerical simulation is defined as $\omega_d(t) := \pi/3 \text{ rad/s}$, $\tau_1 := 3 \text{ s}$ based on the experimental setup.

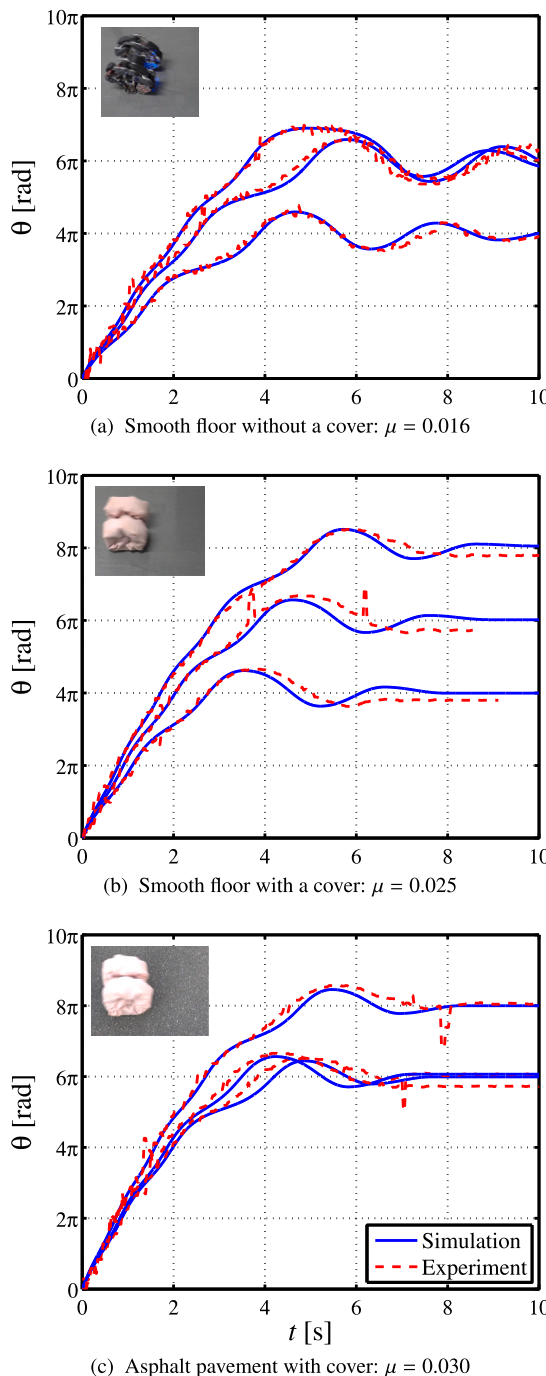


Fig. 9. Comparison of the time-series of the rolling angle $\theta(t)$ for three trials of the free-rolling motion between the experimental and numerical analyses under the identified rolling friction coefficient on (a) the smooth floor without a waterproof cover: $\mu = 0.016$, (b) the smooth floor with a waterproof cover: $\mu = 0.025$, and (c) the asphalt pavement with a waterproof cover: $\mu = 0.030$.

The kick-only motion [Case 1] fails the rolling movement because the reverse rotation is generated by the COG motion during the motion transition: (a) → (c) as illustrated in Fig. 10. In [Case 2] with the COG shift I, the rotational motion does not continue, except for the non-friction condition: $\mu = 0$ with the timing of the kick motion: $\theta_{\max} = \pi$ rad (Fig. 10(a)). This is because the rotational motion stops owing to the frictional force during the free rotation: (c), and therefore, transition to the next motion stage is not possible. In [Case 2], if the timing of the kick motion is $\theta_{\max} > \pi$ rad, the rotational motion continues even in the

Table 2

Experimental conditions for the sidewinding locomotion.

No.	$u_{\max,v}$ [Nm]	$u_{\max,h}$ [Nm]	f [Hz]	$\Delta\psi$ [rad]
1	8.0	15.0	0.5	$\pi/2.5$
2	8.0	15.0	0.5	$\pi/3.0$
3	8.0	15.0	0.5	$\pi/3.5$

presence of frictional forces (Fig. 10(b)–10(d)). In particular, under the condition of $\theta_{\max} \geq 5/4\pi$ rad, rotational motion is maintained even at a large rolling-friction coefficient $\mu = 0.070$ (Figs. 10(c) and 10(d)).

5. Experiments

We conducted an experiment to compare the movement efficiency between the above-mentioned sidewinding movement and the proposed COG-shift rolling motion as the movement of the snake-like robot.

5.1. Experimental setup

The experimental environment is illustrated in Fig. 11. The distance between the starting and goal lines on the smooth floor is 1.214 m, which is equivalent to four tiles of approximately 30 cm length on each side; therefore, the sidewinding motion would be more than two cycles and within the range of the video camera on the tripod. The time histories of the input torque, joint angles, joint angular velocity, and consumed power of the snake-like robot during the sidewinding motion were logged by the MCU mounted in the head and tail links. A movie of the sidewinding experiment was recorded using a video camera (DSC-RX10M4, Sony Corp., Japan) at a resolution of 3840 × 2160 with a frame rate of 24 fps.

The proposed rolling motion was also evaluated on the smooth floor by logging the consumed power and rolling angle.

5.2. Experimental procedure

The procedure of the sidewinding motion experiment is illustrated from [Step 1] to [Step 6].

- [Step 1] Place the snake-like robot at the start line.
- [Step 2] Start recording using the video camera.
- [Step 3] Start the sidewinding motion and start logging the power-consumption data.
- [Step 4] Visually confirm that the robot has reached the goal line, and stop the sidewinding motion and logging the power consumption data.
- [Step 5] End the recording of the video camera.
- [Step 6] Repeat from [Step 1] to [Step 5] ten times.

The experimental conditions for the sidewinding locomotion are displayed in Table 2. For sidewinding motion, the average speed V was calculated by dividing the distance 1.214 m by the drive time recorded by the MCU. The time history of the power consumption at the head and tail section $P_{\text{head}}(t)$, $P_{\text{tail}}(t)$ was time-averaged with the drive time T_{drive} to calculate the following time-averaged power consumption P_{in} ,

$$P_{\text{in}} := \frac{1}{T_{\text{drive}}} \int_0^{T_{\text{drive}}} \{ P_{\text{head}}(t) + P_{\text{tail}}(t) \} dt, \quad (25)$$

$$P_{\text{head}}(t) := \sum_{m=1}^{N_{\text{servo}}} V_{\text{in},m}(t) I_{\text{in},m}(t), \quad (26)$$

$$P_{\text{tail}}(t) := \sum_{m=N_{\text{servo}}+1}^{2N_{\text{servo}}} V_{\text{in},m}(t) I_{\text{in},m}(t), \quad (27)$$

where $V_{\text{in},m}$ and $I_{\text{in},m}$ are the voltage and current measured in the m th servomotor, respectively.

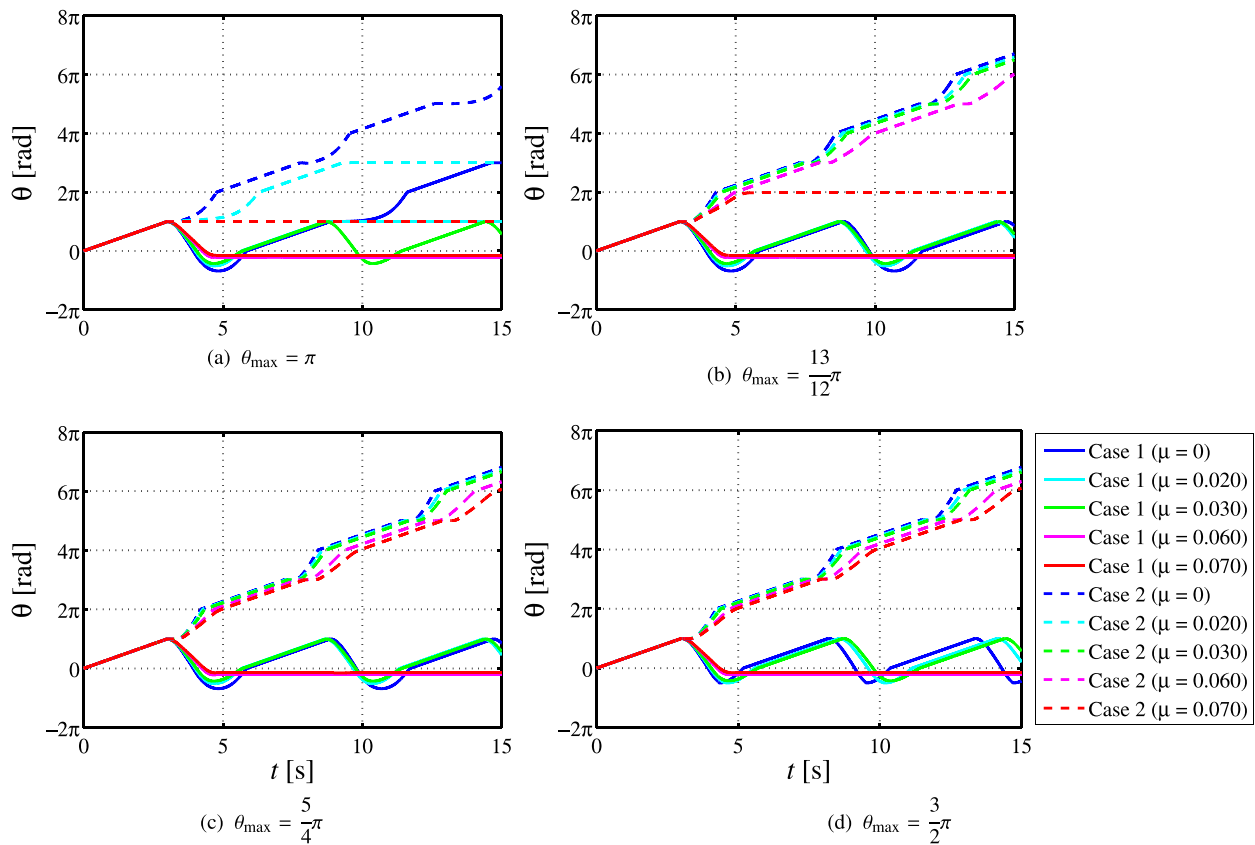


Fig. 10. Comparison of the time-series of the rolling angle $\theta(t)$ obtained by numerical analysis under two kinds of motion transitions; [Case 1] and [Case 2], various rolling friction coefficients μ , and timings of the kicking motion θ_{\max} .

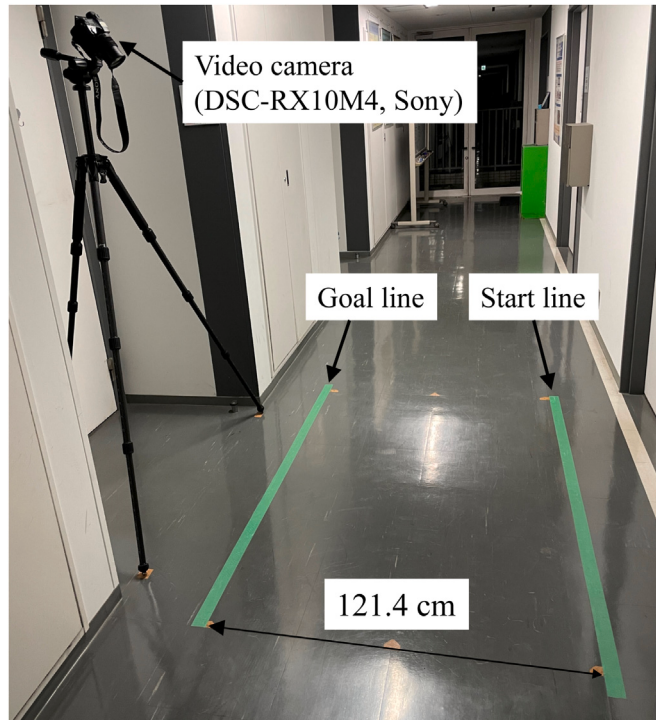


Fig. 11. Experimental setup for the sidewinding motion. Distance between the start line and goal line is 1.214 m.

For rotational movement, a value of $\theta_{\max} = 5\pi/4$ rad was used for the timing of the kick movement, which is robust against large rolling friction coefficients μ based on the numerical analysis shown in Section 4.3. The distance traveled was calculated from $R\theta_o$ using the recorded rolling angle θ_o and radius $R = 0.130$ m.

6. Results and discussion

The experimental results of the time-averaged power consumption P_{in} and time-averaged velocity V in three sidewinding motions with different phase differences $\Delta\psi$ and the proposed rolling motion are illustrated in Fig. 12. The time-series of the power consumed in the head and tail sections in the sidewinding ($f = 0.5$ Hz, $\Delta\psi = \pi/3.0$ rad) and rolling motion are illustrated in Fig. 13.

6.1. Speed and consumed power

The closed circle markers represent the experimental results of the sidewinding motion, and the square markers represent the results of the rolling motion in Fig. 12. The error bars represent the standard deviation of ten trials in the experiment. Red, blue, and green open circles represent the experimental results under rolling around the body axis, sidewinding, and linear progression reported in the preceding study with the no-wheeled snake-like robot[19] for comparison, respectively.

In the rolling motion proposed in this study, the moving speed is $V \approx 0.22$ m/s, which is similar to the maximum speed of $V \approx 0.26$ m/s in the sidewinding motion under the condition in Table 2. In the time-averaged power consumption P_{in} for the movement, the one for the rolling motion is $P_{in} \approx 26$ W, which is approximately half of $P_{in} > 40$ W for the sidewinding movement.

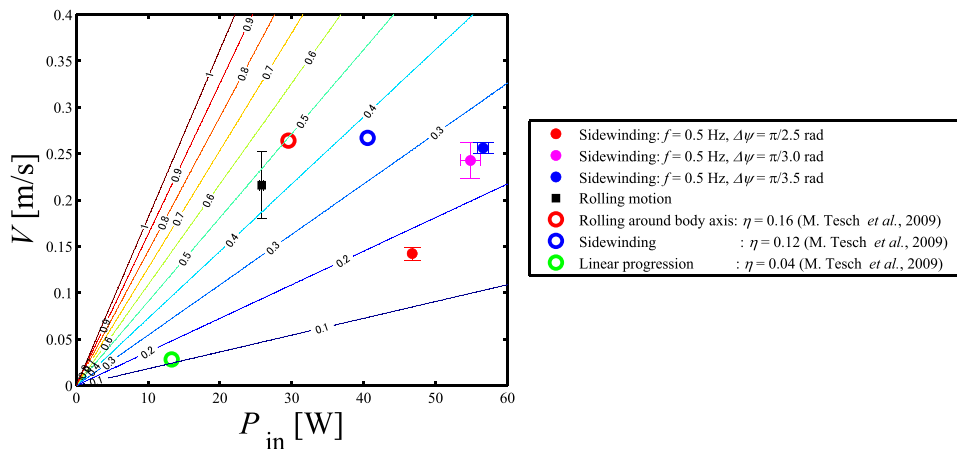


Fig. 12. Comparison of the traveling efficiency between the sidewinding and the rolling motion in the experiments. The error bar represents the standard deviation of the time-averaged consumed power P_{in} and velocity V with the measured data pertaining to the ten trials. Contour lines represent the traveling efficiency η . Red, blue, and green open circles represent the experimental results under rolling around the body axis, sidewinding, and linear progression reported in the preceding study[19], respectively. Moreover, the traveling efficiency η is shown in the legend because the total mass is $M = 1.8 \text{ kg}$, which differs from that of our model.

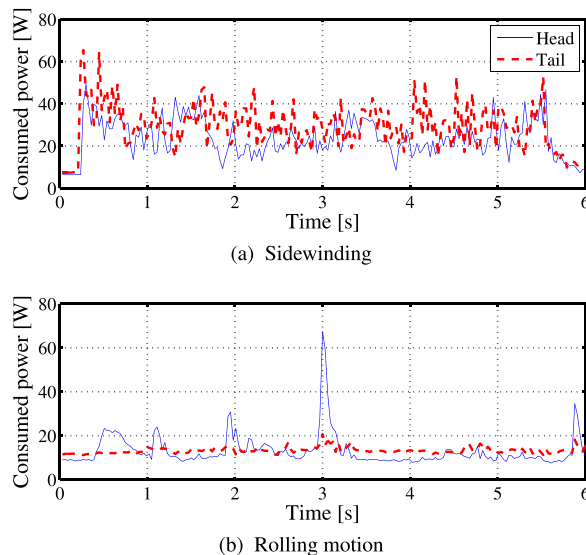


Fig. 13. Comparison of the time-series of the consumed power $P_{\text{head}}(t)$, $P_{\text{tail}}(t)$ shown in Eqs. (26) and (27) between the sidewinding ($f = 0.5 \text{ Hz}$, $\Delta\psi = \pi/3.0 \text{ rad}$) and the rolling motion in the experiments. The blue solid and red dashed lines represent the power consumed in the head section and tail section, respectively.

As indicated by red and blue open circles, the rolling around the body axis and sidewinding in the preceding study indicates good traveling speed per unit consumed power; however, the total mass of this robot ($M = 1.8 \text{ kg}$) is lower than our experimental model ($M = 5.63 \text{ kg}$).

Focusing on the time-series of the power consumption $P_{\text{head}}(t)$ and $P_{\text{tail}}(t)$ in Fig. 13, we can observe that the sidewinding motion (Fig. 13(a)) consumes a large amount of power over the entire drive duration. Conversely, for the rolling motion (Fig. 13(b)), the tail section consumes less than 20 W, whereas the consumed power in the head section shows an impulse-like peak. This is because only one wheel-shaped link is driven to generate the rolling motion, as illustrated in Fig. 5, which contributes to the overall reduction in power consumption.

6.2. Motion efficiency

The number on the contour line in Fig. 12 represents the traveling efficiency η , which is defined by the following equation:

$$\eta := \frac{M g V}{P_{\text{in}}} \quad (28)$$

For the sidewinding motion, the efficiency of the movement is $\eta < 0.26$, whereas it is $\eta \approx 0.46$ for the rolling motion. This is because, as mentioned above, the power consumption in the rolling motion is nearly half that of the sidewinding motion.

In a previous study [19], the traveling efficiency η is shown in the legend because the total mass is $M = 1.8 \text{ kg}$ which differs from that of our model. The traveling efficiency η under rolling around the body axis, sidewinding, and linear progression reported in the previous study is lower than 0.2 because these motions need to drive all servomotors.

The previous studies on the wheeled snake-like robot demonstrate more efficient traveling on flat ground ($\eta > 1$)[21,22]. However, the snake-like robot with small passive wheels is somewhat less adaptable to environmental changes; for example, their mobility gets affected in rough ground and muddy water.

Therefore, compared with the undulating motion and other motions reported in the previous study with the no-wheeled snake-like robot, the proposed rolling motion can achieve a higher traveling efficiency on flat ground. In addition, by switching to undulation, it can be applied to swimming in the water and traveling on rough ground, as in previous studies on the no-wheeled snake-like robots.

6.3. Energy consumption in transformation process

Fig. 14 shows the time-series of the energy consumption (shown in Fig. 14(a)) and the relative joint angles (shown in Fig. 14(b)) in the transformation process. The durations indicated in cyan, yellow, magenta, and blue correspond to the transformation stage from the undulation to the rolling motion, rolling motion stage, transformation stage from the rolling motion to the undulation, and undulation stage, respectively. Moreover, the blue solid and red dashed lines represent the consumed power and the relative joint angles of servomotors in the head and tail sections, respectively.

As shown in the cyan domain in Fig. 14(a), the consumed power in the transformation process from the undulation to the rolling motion is approximately 30 W, and the time duration for the transformation process is approximately 14 s. On the other hand, the consumed power in the transformation process from the rolling motion to the undulation is approximately 20 W, and the time duration for the transformation process is approximately 1–2 s which is significantly smaller than that of above-mentioned transformation process, as shown in the magenta domain.

Therefore, the energy consumption in the transformation process from the undulation to the rolling motion is more significant than the one from the rolling motion to the undulation, and the energy

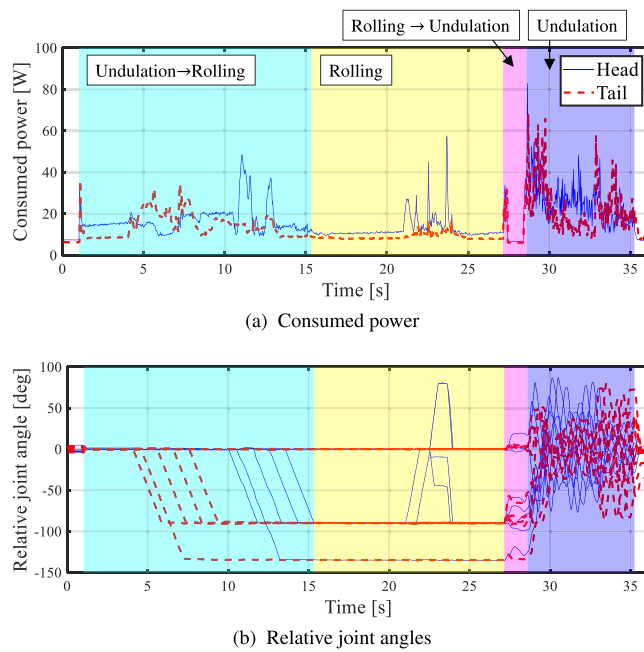


Fig. 14. The time-series of (a), energy consumption, and (b) relative joint angles in the transformation process. The durations indicated in cyan, yellow, magenta, and blue correspond to the transformation stage from the undulation to the rolling motion, rolling motion stage, transformation stage from the rolling motion to the undulation, and undulation stage, respectively. The blue solid and red dashed lines represent the consumed power and relative joint angles of servomotors in the head and tail sections, respectively.

consumption for all servomotors is approximately $E_{\text{transform}} \simeq 30 \times 14 = 420\text{J}$. Therefore, to obtain the merit for the proposed rolling motion in view of traveling efficiency, the time duration of the rolling motion should be

$$\begin{aligned} \eta &= \frac{MgVT_{\text{drive}}}{P_{\text{in}}T_{\text{drive}} + E_{\text{transform}}} > 0.26, \\ \Leftrightarrow (MgV - 0.26P_{\text{in}})T_{\text{drive}} &> 0.26E_{\text{transform}}, \\ \Leftrightarrow T_{\text{drive}} &> \frac{0.26E_{\text{transform}}}{MgV - 0.26P_{\text{in}}} \\ &= \frac{0.26 \cdot 420}{5.63 \cdot 9.81 \cdot 0.216 - 0.26 \cdot 25.8} \\ &\simeq 21\text{s}. \end{aligned} \quad (29)$$

7. Conclusions

In this study, we proposed a new method for snake-like robots to efficiently move on flat terrain by transforming the snake-like robot into a two-wheeled form using the COG shift. First, a method for transforming a snake-like robot into a two-wheeled robot is presented. Next, we presented a method for generating a rolling motion by shifting the COG in the wheeled form. The simplified equations of motion for the proposed motion were presented, and the validity of the model was demonstrated by comparing the experimental and numerical results under different friction environments. Furthermore, the model was used to study the appropriate timing of the COG shift. Finally, experiments were conducted to evaluate the traveling efficiency of the conventional side-winding and the rolling motion with the proposed COG shift. The results obtained above can be summarized as follows:

- For the timing of the motion transition of the COG shift, it is necessary that $\theta_{\max} > \pi$ rad for the rolling motion. Especially, for a large rolling-friction coefficient $\mu \geq 0.07$, and $\theta_{\max} \geq 5\pi/4$ rad for the rolling motion.

- We observed that, on a flat smooth ground, the method of movement proposed in this paper can maintain almost the same speed as the conventional sidewinding locomotion, while consuming only half the power.

On flat terrain, the proposed drive method is expected to enable the snake-like robot to operate for a longer period of time than conventional snake-like robots with wireless communication, resulting in a large battery-capacity limitation.

In this study, we searched for appropriate drive conditions to realize the rolling motion based on two types of COG trajectories and four types of kick motion timings under the experimental setup's parameters that enable forward and backward rolling motion. In the future, the realization of turning motion, design of a more optimal COG trajectory than that in the present study, and the density distribution of the tire-shape body should be studied.

CRediT authorship contribution statement

Akio Yamano: Conceptualization, Funding acquisition, Methodology, Software, Supervision, Validation, Visualization, Investigation, Writing – original draft. **Yuuki Ikeda:** Data curation, Investigation, Writing – review & editing. **Keita Imai:** Data curation, Investigation, Writing – review & editing. **Masakatsu Chiba:** Resources, Writing – review & editing.

Declaration of competing interest

The authors declare that they have no known competing financial interests or personal relationships that could have appeared to influence the work reported in this paper.

Data availability

No data was used for the research described in the article.

Acknowledgments

This study was supported by a The Mazda Foundation, Japan. We would like to thank Editage (www.editage.com) for English-language editing.

Appendix A. Supplementary data

Supplementary material related to this article can be found online at <https://doi.org/10.1016/j.mechatronics.2023.103024>.

References

- [1] Enner F, Rollinson D, Choset H. Motion estimation of snake robots in straight pipes. In: 2013 IEEE international conference on robotics and automation. 2013, p. 5168–73. <http://dx.doi.org/10.1109/ICRA.2013.6631316>.
- [2] Sato M, Fukaya M, Iwasaki T. Serpentine locomotion with robotic snakes. IEEE Control Syst Mag 2002;22(1):64–81. <http://dx.doi.org/10.1109/37.980248>.
- [3] Transteth AA, Pettersen KY, Liljeback P. A survey on snake robot modeling and locomotion. Robotica 2009;27(7):999–1015. <http://dx.doi.org/10.1017/S0263574709005414>.
- [4] Matsumoto N, Tanaka M, Nakajima M, Fujita M, Tadakuma K. Development of a folding arm on an articulated mobile robot for plant disaster prevention. Adv Robot 2020;34(2):89–103. <http://dx.doi.org/10.1080/01691864.2019.1689167>.
- [5] Gray J. The mechanism of locomotion in snakes. J Exp Biol 1946;23(2):101–20. <http://dx.doi.org/10.1242/jeb.23.2.101>.
- [6] Hirose S, Cave P, Goulden C. Biologically inspired robots: Snake-like locomotors and manipulators. Oxford science publications, Oxford University Press; 1993.
- [7] Ijspeert AJ, Crespi A. Online trajectory generation in an amphibious snake robot using a lamprey-like central pattern generator model. In: Proceedings 2007 IEEE international conference on robotics and automation. 2007, p. 262–8. <http://dx.doi.org/10.1109/ROBOT.2007.363797>.

- [8] Transeth AA, Leine RI, Glocker C, Pettersen KY, Liljeback P. Snake robot obstacle-aided locomotion: Modeling, simulations, and experiments. *IEEE Trans Robot* 2008;24(1):88–104. <http://dx.doi.org/10.1109/TRO.2007.914849>.
- [9] Transeth AA, Leine RI, Glocker C, Pettersen KY. 3-D snake robot motion: Nonsmooth modeling, simulations, and experiments. *IEEE Trans Robot* 2008;24(2):361–76. <http://dx.doi.org/10.1109/TRO.2008.917003>.
- [10] Kelasidi E, Liljeback P, Pettersen KY, Gravdahl JT. Experimental investigation of efficient locomotion of underwater snake robots for lateral undulation and eel-like motion patterns. *Robotics Biomim* 2015;2:1–27. <http://dx.doi.org/10.1186/s40638-015-0029-4>.
- [11] Yamano A, Shimizu K, Chiba M, Ijima H. Fluid force identification acting on snake-like robots swimming in viscous fluids. *J Fluids Struct* 2021;106(103351). <http://dx.doi.org/10.1016/j.jfluidstructs.2021.103351>.
- [12] Jia Y, Ma S. A coach-based Bayesian reinforcement learning method for snake robot control. *IEEE Robot Autom Lett* 2021;6(2):2319–26. <http://dx.doi.org/10.1109/LRA.2021.3061372>.
- [13] Takemori T, Tanaka M, Matsuno F. Hoop-passing motion for a snake robot to realize motion transition across different environments. *IEEE Trans Robot* 2021;37(5):1696–711. <http://dx.doi.org/10.1109/TRO.2021.3063438>.
- [14] Kurokawa H, Kamimura A, Yoshida E, Tomita K, Murata S, Kokaji S. Self-reconfigurable modular robot (M-TRAN) and its motion design. In: International conference on control, automation, robotics and vision. 2002, p. 51–6. <http://dx.doi.org/10.1109/ICARCV.2002.1234789>.
- [15] Zhao J, Cui X, Zhu Y, Tang S. A new self-reconfigurable modular robotic system UBot: Multi-mode locomotion and self-reconfiguration. In: 2011 IEEE international conference on robotics and automation. 2011, p. 1020–5. <http://dx.doi.org/10.1109/ICRA.2011.5980293>.
- [16] Wang X, Jin H, Zhu Y, Chen B, Bie D, Zhang Y, et al. Serpentoid polygonal rolling for chain-type modular robots: A study of modeling, pattern switching and application. *Robot Comput-Integr Manuf* 2016;39:56–67. <http://dx.doi.org/10.1016/j.rcim.2015.12.003>.
- [17] Astley H, Gong C, Dai J, Travers M, Serrano M, Vela P, et al. Modulation of orthogonal body waves enables high maneuverability in sidewinding locomotion. *Proc Natl Acad Sci USA* 2015;112(19):6200–5. <http://dx.doi.org/10.1073/pnas.1418965112>.
- [18] Marvi H, Gong C, Gravish N, Astley H, Travers M, Hatton R, et al. Sidewinding with minimal slip snake and robot ascent of sandy slopes. *Science* 2014;346(6206):224–9. <http://dx.doi.org/10.1126/science.1255718>.
- [19] Tesch M, Lipkin K, Brown I, Hatton R, Peck A, Rembisz J, et al. Parameterized and scripted gaits for modular snake robots. *Adv Robot* 2009;23(9):1131–58. <http://dx.doi.org/10.1163/156855309X452566>.
- [20] Ariizumi R, Matsuno F. Dynamic analysis of three snake robot gaits. *IEEE Trans Robot* 2017;33(5):1075–87. <http://dx.doi.org/10.1109/TRO.2017.2704581>.
- [21] Ute J, Ono K. Fast and efficient locomotion of a snake robot based on self-excitation principle. In: The 7th international workshop on advanced motion control. Proceedings. 2002, p. 532–9. <http://dx.doi.org/10.1109/AMC.2002.1026977>.
- [22] Kakogawa A, Kawabata T, Ma S. Plate-sprung parallel elastic actuator for efficient snake robot movement. *IEEE/ASME Trans Mechatronics* 2021;26(6):3051–63. <http://dx.doi.org/10.1109/TMECH.2021.3052037>.



Akio Yamano received B.Eng., M.Eng., and Ph.D. degrees in mechanical engineering from Osaka Prefecture University, Osaka, Japan, in 2012, 2014, and 2017, respectively. Since 2022, he has been an assistant professor at the Department of Aerospace Engineering, Graduate School of Engineering, Osaka Metropolitan University. His research interests include fluid-structure interaction, design of flexible robots, and self-excited oscillators.



Yuuki Ikeda received B.Eng. degrees in aerospace engineering from Osaka Prefecture University, Osaka, Japan, in 2021. His research interests include flexible robots.



Keita Imai received B.Eng. degrees in aerospace engineering from Osaka Prefecture University, Osaka, Japan, in 2020. His research interests include flexible robots.



Masakatsu Chiba received M.Eng. and D.Eng. in Mechanical Engineering from Tohoku University, Sendai, Japan in 1981 and 1985, respectively. Since 2005, he has been a Professor of aerospace engineering at the Osaka Prefecture University. On April 2022, he is a Professor emeritus. His research interests include the fluid-coupled dynamics of flexible structures, such as vibration of large flexible spacecraft and non-linear vibration of liquid storage tanks, in terms of both theoretical and experimental aspects.